The Astrophysical Journal, 908:111 (12pp), 2021 February 10 https://doi.org/10.3847/1538-4357/abce5c

Detection of Energy Cutoffs in Flare-accelerated Electrons

Fanxiaoyu Xia[1,2], Yang Su[1,2], Wen Wang[3], Linghua Wang[3], Alexander Warmuth[4], Weiqun Gan[1,2], and Youping Li[1,2]
[1] Key Laboratory of Dark Matter and Space Astronomy, Purple Mountain Observatory, Chinese Academy of Sciences, Nanjing 210023, People's Republic of China
yang.su@pmo.ac.cn
[2] School of Astronomy and Space Science, University of Science and Technology of China, Hefei 230026, People's Republic of China
[3] School of Earth and Space Sciences, Peking University, Beijing, 100871, People's Republic of China
[4] Leibniz-Institut für Astrophysik Potsdam (AIP), An der Sternwarte 16, D-14482 Potsdam, Germany

Received 2020 June 23; revised 2020 November 8; accepted 2020 November 24; published 2021 February 17

Abstract

Energy cutoffs in electron distribution define the lower and upper limits on the energy range of energetic electrons accelerated in solar flares. They are crucial parameters for understanding particle acceleration processes and energy budgets. Their signatures have been reported in studies of flattened flare X-ray spectra, i.e., the impulsive emission of nonthermal bremsstrahlung from energetic electrons impacting ambient, thermal plasma. However, these observations have not provided unambiguous constraints on the cutoffs. Moreover, other processes may result in similar spectral features. Even the existence and necessity of cutoffs as physical parameters of energetic electrons have been under debate. Here we report a search for their signatures in flare-accelerated electrons with two approaches, i.e., in both X-ray spectra and solar energetic particle (SEP) events. These represent two different electron populations, but may contain information of the same acceleration process. By studying a special group of late impulsive flares, and a group of selected SEP events, we found evidence of cutoffs revealed in both X-ray spectra and SEP electron distributions. In particular, we found for the first time consistent low- and high-energy cutoffs in both hard X-ray-producing and escaping electrons in two events. We also showed the importance of high-energy cutoff in studies of spectral shapes. These results provide evidence of cutoffs in flare-accelerated energetic electrons and new clues for constraining electron distribution parameters and particle acceleration models.

Unified Astronomy Thesaurus concepts: Solar x-ray flares (1816); X-ray telescopes (1825); Solar x-ray emission (1536); Solar flares (1496); Solar flare spectra (1982)

1. Introduction

Solar flare X-ray bursts usually consist of two types of bremsstrahlung emission (e.g., Brown 1971; Holman et al. 2011; Benz 2017), i.e., thermal emission from heated plasma and nonthermal emission from energetic electrons. The nonthermal components are often seen as power-law or broken power-law spectra, produced by electrons that are predominantly accelerated during magnetic reconnection processes in flares. Therefore, analysis of X-ray emission produced by them is an important tool for understanding the physical processes in flares (see the reviews of Krucker et al. 2008; Hudson 2011; Zharkova et al. 2011; Raymond et al. 2012), such as magnetic reconnection, plasma heating, waves, particle acceleration, and particle transport.

In the diagnostics of X-ray spectra, the low-energy cutoff E_{lc} in a power-law electron distribution is the most critical and sensitive parameter that determines total number of energetic electrons and total energy carried by them. The total electron flux is obtained by

$$F_{\mathrm{tot}} = \int_{E_{\mathrm{lc}}}^{E_{\mathrm{hc}}} F_0(E_e)\, dE_e = A \int_{E_{\mathrm{lc}}}^{E_{\mathrm{hc}}} E_e^{-\delta}\, dE_e, \tag{1}$$

where $F_0(E_e)$ is the differential electron flux, E_{lc} the low-energy cutoff, and E_{hc} the high-energy cutoff. Since $F_0(E_e)$ often takes the form of a power law with an index $\delta > 2$, a low-energy cutoff is mathematically required to keep the total flux finite. Cutoffs are also predicted by theory stipulating that electrons are accelerated out of the tail of the thermal distribution, down to the lowest particle energy for which the acceleration mechanism can overcome the collisional force. Examples for this are DC acceleration in a 3D reconnecting current sheet (e.g., Zharkova & Gordovskyy 2005) and shock-drift acceleration at a termination shock (e.g., Warmuth et al. 2009b). As shown in Figure 1, whether the cutoff is a sharp one or a turnover (e.g., Saint-Hilaire & Benz 2005; Holman et al. 2011), its existence causes the emitted X-ray spectrum to be significantly flattened at energies below the cutoff energy, with a decreasing power-law photon spectral index γ to as low as $\sim$1.3 (in the case for a sharp cutoff, see Figure 1). This particular spectral break is a strong signature of low-energy cutoff that can be found in some observed X-ray spectra.

However, in most cases, the thermal emission from flare-heated plasma usually dominates at energies of soft X-rays and the lower end of hard X-rays (HXRs), thus masking the signature of a flattened nonthermal component. The values derived from spectral analysis are therefore often merely upper limits of the low-energy cutoff (e.g., Holman 2003). Besides, there are other processes that may produce flattened spectra, although these flattenings are usually not as flat as the one caused by E_{lc}. These include an additional albedo component reflected by the photosphere (e.g., Kontar et al. 2006; Kašparová et al. 2007), high-energy cutoffs (e.g., Holman 2003), return-current energy losses (e.g., Knight & Sturrock 1977; Zharkova & Gordovskyy 2006; Holman 2012; Alaoui & Holman 2017),

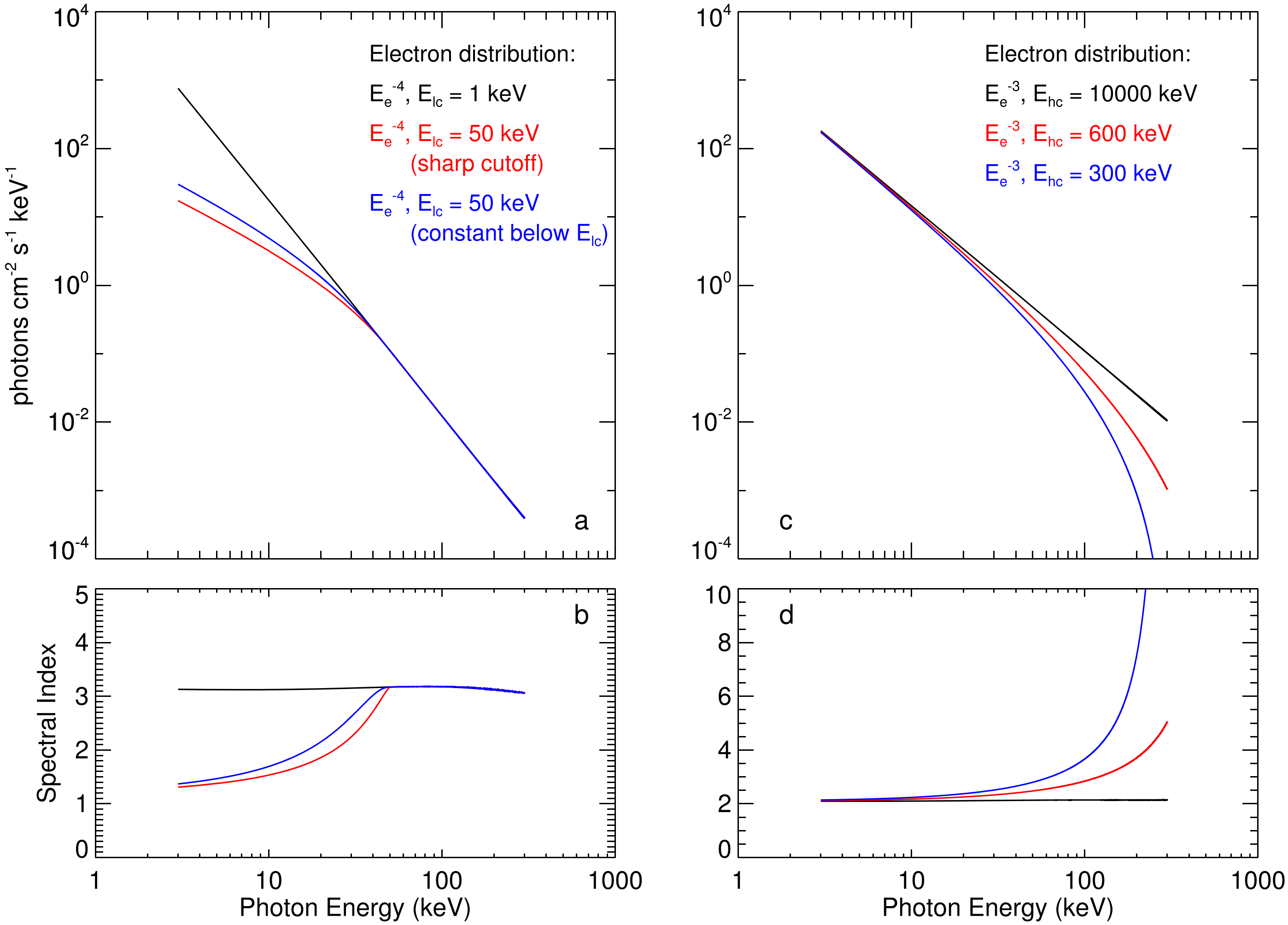

Figure 1. This figure shows the effects of low- and high-energy cutoffs in electron distributions on the corresponding bremsstrahlung photon spectral shape. Panel (a): thick-target bremsstrahlung photon spectra from electron distributions with high-energy cutoffs fixed at 10 MeV and low-energy cutoffs at 1 keV (black curve), 50 keV (sharp cutoff, red curve), and 50 keV (electron distribution is a constant equal to $F\,(E_e = 50)$ below 50 keV, blue curve). Panel (c): thick-target bremsstrahlung photon spectra for electron distributions with low-energy cutoffs fixed at 1 keV and high-energy cutoffs at 300 keV (blue curve), 600 keV (red curve), and 10 MeV (black curve). Panels (b) and (d): spectral index as a function of photon energy derived from the photon spectra in panels (a) and (c).

nonuniform target ionization (e.g., Brown 1973; Kontar et al. 2002; Su et al. 2009), extra super-hot component, pulse pile-up effects, etc. Therefore, it has not been confirmed whether low-energy cutoff directly resulting from the acceleration mechanism really exists.

Another argument was raised that other forms such as kappa distribution, which combines a Maxwellian-like distribution and a power-law tail without the need of introducing a low-energy cutoff, may be a more natural representation for electron distributions. In fact, some authors (e.g., Kašparová & Karlický 2009; Oka et al. 2013, 2015; Battaglia et al. 2015) have successfully applied kappa distribution to flare X-ray studies. However, for that very reason, a flattened spectrum that is indeed caused by a low-energy cutoff cannot be easily explained by a single kappa distribution. So the question remains, does low-energy cutoff really exist in accelerated electrons?

Many studies reported or assumed a low-energy cutoff around 20 keV. For example, Christe et al. (2008) made a statistical study of microflares and found that the nonthermal energies calculated using assumed $E_{\rm lc}$ at 15 keV are comparable to that in earlier studies; Sui et al. (2005) found that the low-energy cutoff should be 24 ± 2 keV to ensure the thermal component dominates at lower energies and makes the time evolution of thermal parameters smooth. However, this is an energy still within the range where thermal emission could easily dominate. There are two types of events that are ideal for the search of $E_{\rm lc}$, early impulsive flares (e.g., Sui et al. 2007) and "cold flares" (e.g., Fleishman et al. 2016). In their spectra during the HXR bursts, the thermal components are relatively less significant, or even negligible. However, studies show that the values of $E_{\rm lc}$ in early impulsive flares are mostly around 20–40 keV, at energies that are still close to the energy range of thermal emissions. This means that the signature of spectral flattening due to a low-energy cutoff may not be fully visible. In the cold flares reported in a recent statistical study (Lysenko et al. 2018), the values of photon spectral index γ_1 of the flattened spectra are above 2 in all the cases, meaning that no full signature was found for $E_{\rm lc}$ (above 20 keV, the starting energy of their fitting range), at least not a clear one.

In order to confirm a low-energy cutoff, the value of $E_{\rm lc}$ (or the break energy in the photon spectrum) should be high enough to allow the flattened part of the spectrum to be fully visible. One of such spectrum was reported in a case study of a late impulsive burst (Warmuth et al. 2009a), where an $E_{\rm lc}$ of ∼100 keV is found. However, in that case, the HXR spectrum is flat and the relatively small spectral break might therefore be explained by other processes. Gan et al. (2002) improved the method of Gan et al. (2001) and analyzed 54 BATSE/CGRO flares. They found that 44% of samples present a lower-energy cutoff varying from 44 to 97 keV, although they took the lower-energy cutoff as the unique cause resulting in a double power law.

Recently, the thick-target model has been extended by including the physics of collisional energy diffusion and thermalization of fast electrons in the heated background plasma that is generated by the flaring process (Kontar et al. 2015). In this warm-target model, the photon spectra generated by an electron beam diverge from those given by the cold-target model, especially at lower energies, with the exact shape and magnitude of the deviation being a function of target temperature and column density. Thus, in the usual case of a masked low-energy cutoff the warm-target model can be used to obtain a lower estimate for the low-energy cutoff (Kontar et al. 2019), because in contrast to the cold-target model, an exceedingly low cutoff would produce an excess of emission due to thermalized electrons. However, in cases where evidence of a spectral flattening can be seen at energies above the thermal component (i.e., $E > 40$ keV), application of the warm target would give very similar results as the cold-target model.

While Aschwanden et al. (2017, 2019) have claimed to apply the warm-target model in order to constrain the energy content in nonthermal electrons, they in fact used an analytical approximation from the model that gives an effective low-energy cutoff. This cutoff was then used as the input for a cold-target fitting. A proper application of the warm-target model might have to involve the determination of the target temperature, density, and length, and therefore requires spectroscopy and imaging (see Kontar et al. 2019).

On the other hand, a high-energy cutoff $E_{\rm hc}$ in electron distribution also affects the shape of X-ray spectra, causing a downward spectral break (toward high energies) and a fast drop-off toward energies close to $E_{\rm hc}$. For example, a high-energy cutoff of 300 keV causes a significant spectral break at energies of the photon ∼100 keV (see Figure 1), which can be effectively taken as spectral flattening at lower energies. In practice, since $E_{\rm hc}$ is not a parameter as sensitive as $E_{\rm lc}$ for determining the total electron flux, it is often set to a fixed value far beyond the X-ray range to minimize its effect on X-ray spectral shape. But like $E_{\rm lc}$, it may also be directly related to acceleration and transport process, and therefore an important physical parameter. However, it is rarely mentioned or considered in spectral studies. One of the reasons is that the decreasing flux at high energies makes the detector background become significant, resulting in a worse signal-to-noise ratio (S/N). Besides, background is extremely difficult to accurately select and remove from observed spectra in some cases. How $E_{\rm hc}$ changes the spectral fitting and affects the parameters of electron distribution remains unanswered.

However, spectral fitting is model-dependent. Different models that give equally good fitting results may coexist (Krucker & Lin 2008). One way of confirming the fitting parameters is to search for consistent evidence of cutoffs from other data, such as solar energetic particle (SEP) electron distribution, which, in some cases, is a direct measurement of energy distribution of escaped electrons in flares. Many studies (e.g., Krucker et al. 2007; Wang et al. 2016) tried to compare the electron distribution derived from the measured SEP electron spectra with the photon spectra from simultaneous X-ray observations. But the focus has been mostly on the electron power-law distribution index. The confirmation of energy cutoffs from both X-ray and SEP particles has not been done before and is therefore one of our motivations.

In this paper, we try to find evidence for the low- and high-energy cutoffs of flare-accelerated electrons in both X-ray spectra and SEP electron distributions.

2. Data Reduction and Processing

We first analyzed a special type of event that occurred at the decay phase of a preceding solar flare. Here we call them late impulsive X-ray bursts. Many of these events show a clear signature of flattened spectra, like the one already reported in Warmuth et al. (2009a).

We selected in total 12 events that show spectral flattening from the Reuven Ramaty High Energy Solar Spectroscopic Imager (RHESSI; Lin et al. 2002) data. The information of all events is listed in Table 1. Most of these events are not recorded as individual flares in the GOES flare list. The GOES classes and peak times in Table 1 refer to the flares preceding the studied late X-ray bursts, and late peak times refer to the late X-ray bursts. RHESSI Detector 3 or 4 was chosen to obtain the X-ray spectra for these events, depending on their status during the flare time. Using a single detector allows us to correct several instrumental effects.

In order to obtain the spectra purely from the late bursts, the backgrounds from preceding flares were carefully determined and subtracted with the help of the OSPEX software package developed from the SPEX (see Schwartz et al. 2002; Ireland et al. 2013). For example, Figures 2(a) and (c) show the light curves of two events (event 5 and 9) whose backgrounds (Figures 2(b) and (d)) were determined by fitting the data in the intervals before and after the late bursts in each energy band individually.

For all the selected events, spectra within a 20 s interval during the late HXR peaks were analyzed using the forward fitting method in OSPEX. Each spectrum was fitted by a number of fitting models, which include a thermal component from the isothermal bremsstrahlung radiation function (f_vth) based on CHIANTI (Landi et al. 2006) and a nonthermal component from the thick-target bremsstrahlung emission function (f_thick2_vnorm) (Brown 1971) or the warm-thick target bremsstrahlung emission function (f_thick_warm) (Kontar et al. 2015). For the warm-thick target models, the thermal parameters of the targets EM and T were derived from the cold-target fitting in the intervals just before the studied HXR peaks, the target volume V and loop length L were estimated from RHESSI images during the HXR bursts, and the density of the targets n were estimated by $n = \sqrt{{\rm EM}/V}$. We corrected the instrumental effects by applying the function f_drm_mod and f_pileup_mod. All fitting models that were used in our study are listed below:

(1) f_vth+f_thick2_vnorm+f_drm_mod+f_pileup_mod ($E_{\rm hc}$ is fixed at a 32 MeV)
(2) f_vth+f_thick2_vnorm+f_drm_mod+f_pileup_mod +f_albedo ($E_{\rm hc}$ is fixed at 32 MeV)

Table 1
Late Impulsive X-Ray Bursts and Two Selected SEP-related Flare Events

Flare index	Date	GOES Class	Peak Time (UT)	Late Peak Time (UT)	$E_{\rm lc1}$ (keV)	$E_{\rm lc2}$ (keV)	$E_{\rm lc3}$ (keV)	Lower $E_{\rm hc}$ (keV)	δ_2	δ_3	Nonthermal Energy (erg)
1	2002 Aug 20	M5.0	01:40	02:08	49.0(±2.6)	53.9(±3.8)	11.6(±20.5)	197.7(±22.4)	4.50	2.67	$>2.76 \times 10^{30}$
2	2002 Sep 8	M1.5	01:43	01:46	38.6(±3.3)	35.3(±3.4)	18.8(±21.0)	371.2(±91.2)	3.71	3.14	2.99×10^{29}
3	2003 Oct 24	M7.6	02:54	06:05	31.6(±1.6)	32.8(±2.4)	29.0(±3.4)	234.8(±61.9)	4.62	4.24	3.29×10^{29}
4	2004 Aug 14	M7.4	05:44	06:32	36.6(±4.8)	37.7(±6.4)	24.8(±14.5)	117.5(±43.1)	5.07	3.30	8.55×10^{27}
5	2004 Aug 14	M2.3	07:56	08:15	51.8(±2.7)	56.0(±4.1)	45.1(±7.4)	195.8(±44.4)	4.73	3.23	2.99×10^{28}
6	2004 Nov 7	X2.0	16:06	16:21	58.1(±1.1)	68.8(±2.0)	60.5(±2.7)	334.6(±57.3)	4.76	3.95	$>1.02 \times 10^{29}$
7	2005 Jan 20	X7.1	07:01	15:19	42.0(±4.3)	42.2(±4.4)	⋯	⋯	4.96	⋯	2.08×10^{28}
8	2005 Nov 19	C1.5	20:19	20:35	40.6(±4.0)	34.3(±4.9)	29.3(±6.3)	173.4(±107.9)	4.48	3.67	8.48×10^{27}
9	2006 Dec 6	X6.5	18:47	19:18	89.0(±4.4)	107.1(±7.1)	41.1(±24.8)	623.5(±163.7)	3.78	2.28	1.25×10^{29}
10	2011 Feb 15	X2.2	01:56	03:19	31.1(±4.4)	27.7(±6.0)	⋯	⋯	3.89	⋯	2.20×10^{28}
11	2011 Feb 24	M3.5	07:35	07:52	53.8(±15.7)	54.5(±16.1)	52.7(±20.0)	360.4(±2125)	4.11	3.70	$>1.49 \times 10^{28}$
12	2015 Apr 16	C5.7	09:07	09:17	34.2(±6.2)	35.0(±8.9)	⋯	⋯	4.06	⋯	4.12×10^{29}
1	2003 Oct 23	M2.4	02:41	⋯	27.2(±1.5)	25.9(±2.2)	23.4(±3.2)	264.0(±71.4)	4.58	4.35	$>3.05 \times 10^{30}$
2	2012 Nov 18	C5.7	04:07	⋯	46.3(±5.5)	46.8(±7.0)	43.2(±9.8)	220.8(±91.6)	4.48	3.74	7.54×10^{28}

Note. (1) GOES classes and peak times refer to the flares preceding the studied late X-ray bursts, and late peak times refer to the late X-ray bursts. (2) The fit parameters are obtained from three models (the low-energy cutoff $E_{\rm lc1}$ from fitting model (1), the low-energy cutoff $E_{\rm lc2}$ and spectral index δ_2 from fitting model (2), and $E_{\rm lc3}$ and $\delta3$ from fitting model (3)). (3) The ">" means that the energies were calculated as lower limits since the HXR bursts in these events were not fully observed.

(3) f_vth+f_thick2_vnorm+f_drm_mod+f_pileup_mod +f_albedo ($E_{\rm hc}$ is free or fixed at the best-fit value)
(4) f_vth+f_thick_warm+f_drm_mod+f_pileup_mod +f_albedo ($E_{\rm hc}$ is fixed at 32 MeV)
(5) f_vth+f_thick_warm+f_drm_mod+f_pileup_mod +f_albedo ($E_{\rm hc}$ is free or fixed at the best-fit value)
(6) f_thick2_vnorm+f_drm_mod+f_pileup_mod+f_albedo ($E_{\rm hc}$ is fixed at 32 MeV).

The function f_albedo was added in fitting models (2)–(6) for albedo correction, since the spectral flattening might result from the albedo effect as reported by Sui et al. (2007) and Kontar et al. (2008). As shown by Holman (2003) and Figure 1, a lower high-energy cutoff and a harder spectral index in electron distribution can also cause the spectral flattening in photon spectra at lower energies. Therefore, $E_{\rm hc}$ was set as a free parameter or fixed at the best-fit value in fitting model (3) and (5), while $E_{\rm hc}$ in other fitting models was fixed at 32 MeV, the default setting.

We used the EUV 171 Å images provided by the Transition Region and Corona Explorer (TRACE; Handy et al. 1999) and the Atmospheric Imaging Assembly (AIA; Lemen et al. 2012) on board the Solar Dynamic Observatory (SDO), and the X-ray images from RHESSI to study the characteristics of sources corresponding to the late X-ray bursts. The X-ray images were reconstructed using a combination of detectors from D3 through D9, and the CLEAN algorithm. Figure 2(e) shows the TRACE EUV image for event 5 in Table 1. During the late peak, there are two jet-like structures, whose footpoints correspond to the HXR sources at energies 25–50 and 50–100 keV. No clear soft X-ray emissions below 10 keV are found in the late burst region, since the emissions are dominated by the preceding flare (at a different location).

In order to describe the thermal components of the late bursts more accurately, we calculated the differential emission measures (DEM) using AIA EUV images and the Sparse code developed by Cheung et al. (2015) with the settings proposed by Su et al. (2018). This method can well constrain plasma DEM at high temperatures above 10 MK and obtain reliable results at temperatures from 0.3 to ∼30 MK in the best cases. Following Su et al. (2018), we calculated the DEMs for each pixel individually in the temperature range of $\log T = 5.5–7.6$ with a logarithmic bin size of 0.05. As an example, Figure 2(f) shows the AIA image of the 2015 April 16 event for the late soft X-ray peak time and RHESSI HXR images at the HXR peak, and Figure 2(g) shows the obtained EM map for the flare region. Since the late burst sources are spatially separated from the preceding flare, we estimated the EMs and areas of the late burst region (Figure 2(g)) rather than the whole flare region. Following Emslie et al. (2012), Li et al. (2012), and Feng et al. (2013), we calculated the total thermal energy by

$$E_{\rm th} = \sum_k 3k_{\rm B}T_k\sqrt{{\rm EM}_k f V_k}\,, \tag{2}$$

where $k_{\rm B}$ is the Boltzmann constant, T_k and ${\rm EM}_k$ are the temperature and the total EM in the late burst region for the kth temperature bin, and f is the volumetric filling factor (we assume $f = 1$ in this paper). The source volume in the kth temperature bin is $V_k = A_k^{3/2}$. A_k represents the area of the late burst region for the kth temperature bin, which includes the pixels whose EMs are above 10% of the peak EM value. Here we only consider thermal plasma whose temperature is above 5 MK. The other two events with AIA data in Table 1 are not discussed here because of the severe saturation or the spatial overlap between the preceding flares and the late bursts.

SEP particles generally have at least two origins: flare-related and CME-related (e.g., Petrosian 2016). Since we only focus on the flare acceleration process here, we neglect any event that may be associated with a CME. We first searched for SEP events corresponding to the late bursts. Unfortunately, we found no such data, although we do see corresponding type III bursts, an indicator of escaping energetic electrons (see the review of Reid & Ratcliffe 2014). In order to find evidence of the energy cutoffs in SEPs, we subsequently selected SEP events that show nearly no enhancement in electron flux below

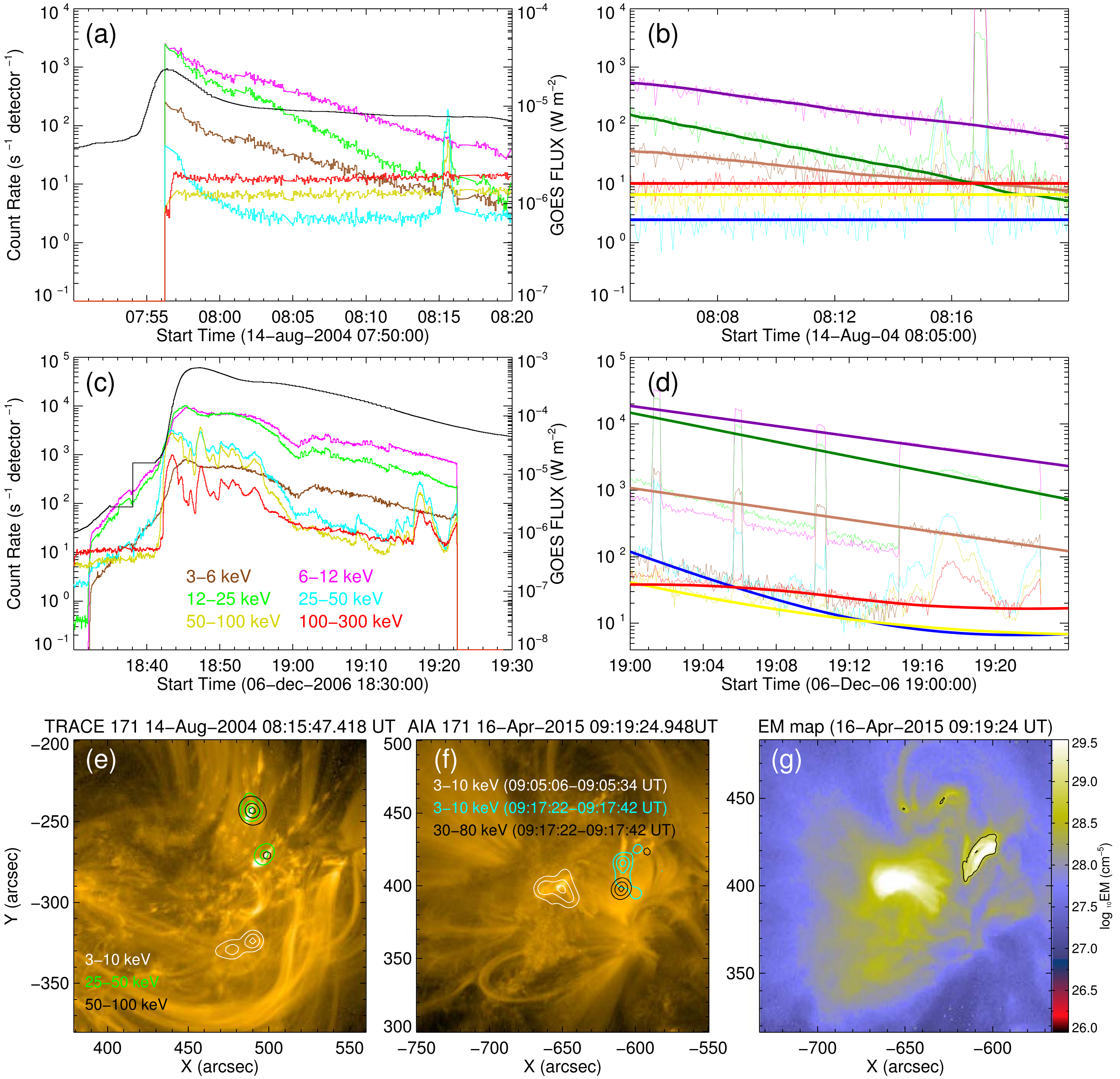

Figure 2. Panels (a) and (c): light curves of GOES flux and RHESSI count rate of the 2004 August 14 event and the 2006 December 6 event. Panels (b) and (d): zoom-ins of the times of interest. The subtracted backgrounds are overplotted on the light curves. Panel (e): TRACE 171 Å image of event 5. The overlaid RHESSI images are integrated over the interval 08:15:22–08:15:42 UT in different energy bands (3–10 keV in white, 25–50 keV in green and 50–100 keV in black). The contour levels are 15%, 60%, 90% for 50–100 keV image, and 30%, 60%, 90% for other images. Panel (f): AIA 171 Å image of the 2015 April 16 event, overlaid by RHESSI contours from the preceding flare (09:05:06–09:05:34 UT) in 3–10 keV (white), and from the late burst (09:17:22–09:17:42) in 3–10 keV (blue) and 30–80 keV (black) at contour levels 30%, 60%, 90%. Panel (g): EM map of the 2015 April 16 event overlaid by 10% contour of the maximum value from late burst region in the map.

27 keV according to the SEP event catalogs observed by the 3D Plasma and Energetic Particle (3DP; Lin et al. 1995) on WIND (compiled by L. Wang; Wang et al. 2012). Then, we selected events that are also accompanied by flares that have flattened HXR spectra. In this way, we finally found two events.

We also obtained the radio dynamic spectra from the Radio and Plasma Wave Experiment (WAVES; Bougeret et al. 1995) on WIND (Lin et al. 1995) and the electron flux from the Wind/3DP. The WIND spacecraft has remained in halo orbits around L1 point since mid 2004 May (Wang 2009). In the onboard 3DP instrument, electron electrostatic analyzers (EESA-L and EESA-H) measure full three-dimensional electron distributions from solar wind plasma to 30 keV with an energy channel resolution of ∼0.2, while silicon semiconductor telescopes measure ∼25–400 keV electron velocity distributions with an energy channel resolution of ∼0.3.

3. Results

3.1. Late Impulsive Bursts

3.1.1. The Low-energy Cutoffs

We first fitted the peak spectra of all events using fitting model (1) and obtained the best-fit low-energy cutoffs E_{lc1} and their uncertainties from OSPEX (Table 1). The low-energy cutoffs are between 31–89 keV and well constrained in most of these events. We plotted the spectra and fitting results for events 5 and 6 as an example (Figure 3). In these two events, the full spectral flattenings at energies below ∼45 and ∼50 keV are clearly observed and can be well fitted by sharp low-energy cutoffs ∼52 and ∼58 keV in single-power-law electron distributions.

The best-fit parameters E_{lc2} and δ_2 in Table 1 are obtained from fitting model (2). We found that for all events, the albedo effects have small impacts on the low-energy cutoffs (E_{lc} even increases in some events, see Figures 3(b) and (d)). Therefore, it is not a viable explanation for the flattened spectra. The albedo correction also increases the uncertainty of E_{lc}. Furthermore, we followed Aschwanden et al. (2019) and checked the $\Delta\chi^2$ ($\Delta\chi^2 = \mathrm{Full}\chi^2 - \min(\chi^2)$) versus E_{lc} for the two events (Figure 3). Both E_{lc1} and E_{lc2} are constrained well, and consistent with results in Table 1.

X-ray imaging provided more evidence to support the existence of E_{lc}. The thermal emission of event 5 is below about 20 keV (see Figures 3(a) and (b)), which means that the photons between 20–50 keV are produced by the energetic electrons with higher energies. This is consistent with the images in Figure 2 and may explain why the HXR sources at different energies appeared at the same location.

The fitting results from the warm-target model (fitting model (4)) are almost consistent with those from fitting model (2) for events 5 and 6 (see Figures 3(e) and (f)), as expected. The thermal component in the interval before the late HXR peak includes significant emission from the preceding flare, which has different locations. In some cases, the thermal component in the late HXR burst is even negligible. Figure 4(a) shows that the spectrum is well-fitted by a nonthermal component alone. This means that the background-subtracted thermal emission is significantly lower than the preceding flare (background). In addition, the high values of the low-energy cutoff in these events mean an absence in lower-energy electrons so that the thermalization may be ignored. We therefore conclude that the use of the warm-target model is not necessary here and opted for using the cold-thick target model to analyze the late burst events.

3.1.2. The High-energy Cutoffs

We introduced a free parameter E_{hc} to fitting model (3) and obtained the best-fit E_{hc} in Table 1. Figures 4(b) and (d) present the examples of the fitting results for two events (5 and 9), the fitting results are slightly better than that from fitting model (2) (see Figures 3(b) and 4(c)). In particular, the residuals are more randomly distributed at high energies (Su et al. 2009).

The large uncertainties might be due to the low S/N and the difficulty in background subtracting at high energies. The high-energy cutoffs in events 7, 10, and 12 cannot be well-determined since they are high enough and their effect (downward spectral breaks at high energies) cannot be observed above the background level. The best-fit parameters E_{lc3} and δ_3 were obtained using fitting model (3) (where the high-energy cutoffs were fixed at the best-fit values).

For most of the events in Table 1 (except events 1 and 2), a lower E_{hc} alone cannot explain the spectral flattening. E_{hc} in events 5, 6, 7, 10, 11, and 12 has nearly no effect on E_{lc}, and the spectral flattening is very likely to result from E_{lc} alone. For other events (events 3, 4, 8, and 9), E_{lc} does decrease but is still above the thermal emission, and the uncertainty of E_{lc} becomes larger. The electron power-law index δ in these events also decreases, meaning a harder electron distribution. Figure 4 shows the fitting results and χ^2 versus E_{lc} of event 5 and 9 as examples. E_{lc} in event 9 decreases to 41.1 keV from 107.1 keV, δ changes from 3.8 to 2.3, and the range of E_{lc} at the 1σ level becomes broader (2.1–52.0 keV from 97.7–115.9 keV) when E_{hc} is fixed at 623.5 keV. Whether the spectral flattening (above 40 keV) in these events should be explained by E_{lc} alone or both E_{lc} and lower E_{hc} is hard to determine. But the effect of high-energy cutoff cannot be ignored.

In the cases of events 1 and 2, the low-energy cutoffs decrease to very low energies and their uncertainties become huge, even the signature of E_{lc} becomes vague when E_{hc} is fixed at a lower value.

3.1.3. The Nonthermal Energies

The nonthermal energies in Table 1 reflect the total nonthermal energies released during the late X-ray bursts. They are calculated using the best-fit parameters from fitting model (2) for each time interval and summing the energies over the duration of the late bursts. It should be noted that some energies were calculated as lower limits since the duration times of these bursts were incomplete due to night time, SAA, or attenuator switch. In addition, these energies will change if fitting model (3) is used (where the spectral index and E_{lc} will change with a lower E_{hc}). However, the change in energy is not significant (the nonthermal energy (power) changes from 6.3×10^{26} to 9.0×10^{26} erg s^{-1} for the 2006 December 6 event).

The low-energy cutoffs in most of these events are higher than the usual values obtained or assumed (20–30 keV). This means that the total number of electrons and the total energy carried by them are significantly small. Perhaps this is the very reason why we do not often see significant thermal emission in these events. We also compared the total nonthermal energy with the thermal energy calculated from DEM analysis for the 2015 April 16 event and found that the nonthermal energy is still in the same order of the peak thermal energy in the late burst (1.1×10^{29} erg).

3.2. SEP Events

Next, we analyzed the electron distributions from both the SEP events and the correlated HXR bursts for the last two flares in Table 1, on 2003 October 23 and 2012 November 18. The SEP electron fluxes and the HXR time profiles of the two events were shown in Figures 5(a) and (d). Figures 5(c) and (f) show the in situ background-subtracted electron distribution at the peak times of the two events, constructed by taking the peak flux of outward-traveling electrons in each energy channel. The simultaneous appearance of the type III burst (as observed by WIND/WAVES) and the HXR burst implies that the flare-accelerated electrons escaped along opened field lines.

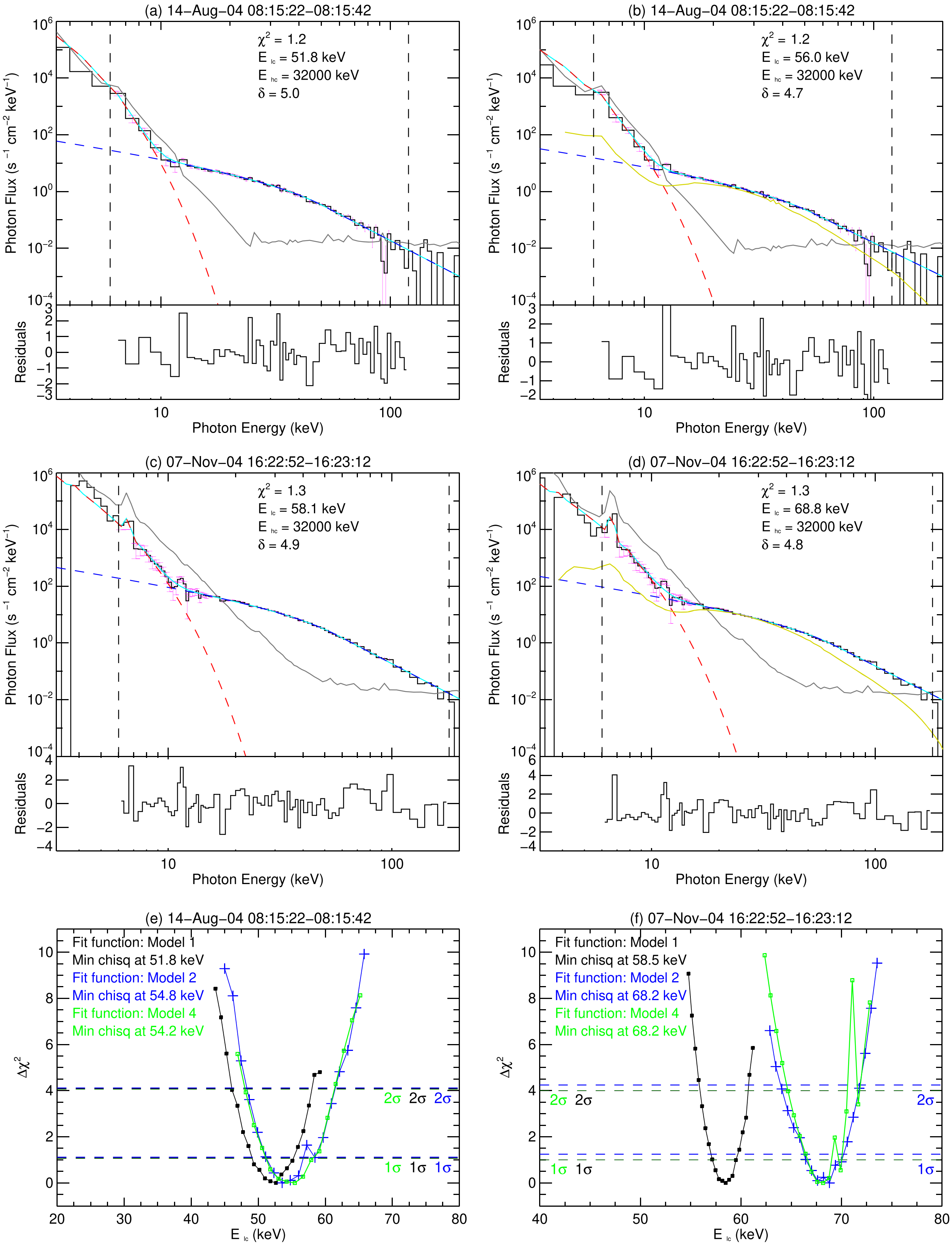

Figure 3. Spectra and fitting results of events 5 and 6. Panels (a) and (c): spectra fitted with fitting model (1) f_vth+f_thick2_vnorm+f_drm_mod+f_pileup_mod. The black histograms are the background-subtracted spectra, the error bars are shown in pink. The gray curves are the backgrounds. The isothermal components are shown by red dashed lines, the nonthermal components are shown by dark blue dashed lines and the full-fitted spectra are shown by light blue lines. The fitting energy ranges are shown by vertical dashed lines. Panels (b) and (d): spectra fitted with fitting model (2) f_vth+f_thick2_vnorm+f_drm_mod+f_pileup_mod+f_albedo. The function f_albedo is shown in yellow. Panels (e) and (f): $\Delta\chi^2$ vs. $E_{\rm lc}$ for the two events under fitting models (1), (2), and (4) f_vth+f_thick_warm+f_drm_mod +f_pileup_mod+f_albedo.

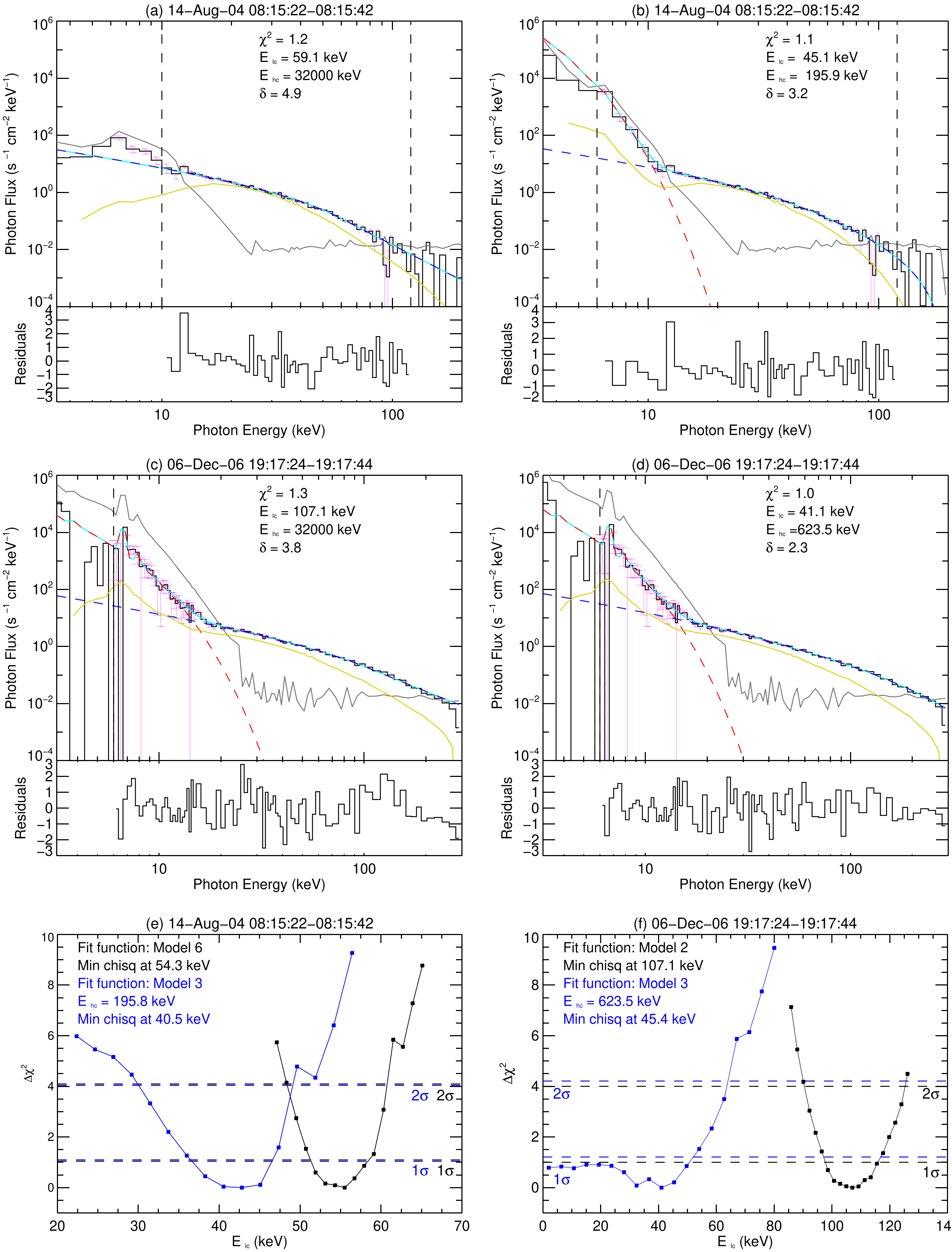

Figure 4. Panels (a) and (b): spectra and fitting results of event 5 using fitting model (6) f_thick2_vnorm+f_drm_mod+f_pileup_mod+f_albedo and fitting model (3) f_vth+f_thick2_vnorm+f_drm_mod+f_pileup_mod+f_albedo (E_{hc} is fixed at the best-fit value). Panels (c) and (d): spectra and fitting results of event 9 using fitting model (2) (f_vth+f_thick2_vnorm+f_drm_mod+f_pileup_mod+f_albedo) and fitting model (3). The fit components are shown in the same way as Figure 3. Panels (e) and (f): $\Delta\chi^2$ vs. E_{lc} for the two events under different fitting models.

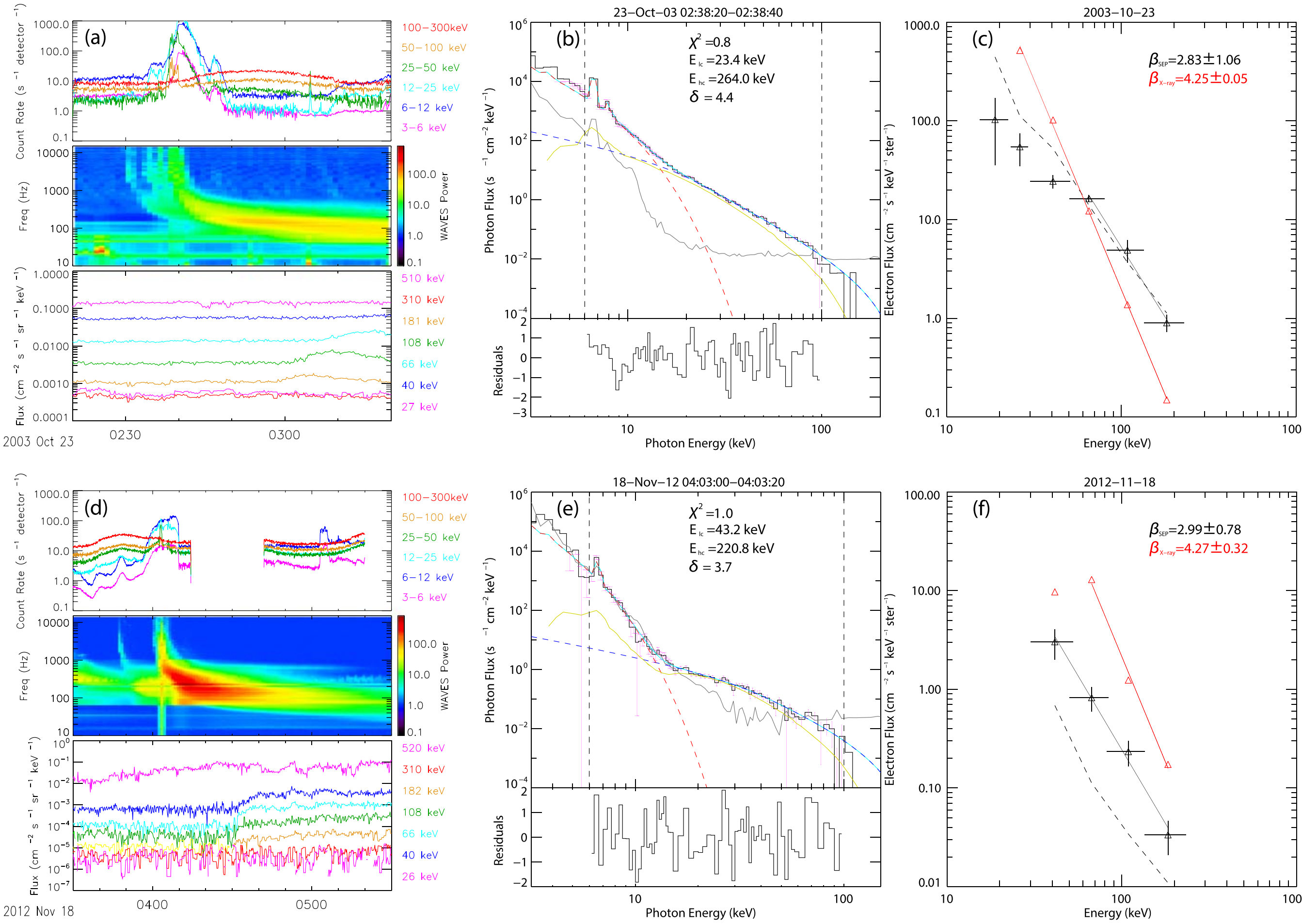

Figure 5. SEP and X-ray information of the 2003 October 23 event and the 2012 November 18 event. Left panels: RHESSI light curves, radio dynamic spectra from WIND/WAVES and time profiles of electron fluxes observed by WIND/3DP (27–510 keV). Middle panels: RHESSI spectra fitted by fitting model (3) f_vth +f_thick2_vnorm+f_drm_mod+f_pileup_mod+f_albedo ($E_{\rm hc}$ is fixed at the best-fit value). Right panels: electron distributions derived from RHESSI HXR spectra (red lines) and SEPs (black lines). The dashed lines represent the backgrounds of SEPs.

As suggested by Wang et al. (2012), an SEP event is selected by the presence of a velocity dispersion of a flux increase at the 2σ level over the background (pre-event background or instrumental background) in at least three energy channels. The energy channels in which the electron fluxes drop to a level lower than the 2σ level of the background are considered as the cutoff energies. The cutoff energies determined from SEPs are dependent on the energy resolution of detectors and the ratio of signal to background. As shown in Figure 5(c), the lower and upper cutoff energies in the in situ electrons are in the ranges of ∼[15, 22] keV and ∼[135, 228] keV for the 2003 October 23 event. The lower and upper cutoff energies of the 2012 November 18 event are ∼[30, 53] keV and ∼[135, 233] keV (Figure 5(f)).

In order to compare the upper and lower cutoff energies detected from SEPs with those obtained from RHESSI spectra, we first fitted the spectra using fitting model (3), with $E_{\rm hc}$ being a free parameter. The best-fit $E_{\rm hc}$ are 264.0 and 220.8 keV for the two events (see Table 1). Their large uncertainties (71.4 and 91.6 keV) are mainly due to the low S/N at high energies (around 100 keV) in these two events. However, the high-energy cutoffs are both close to the upper cutoff energies detected from SEPs (within 1σ range).

Then we fitted the RHESSI spectra using fitting model (3) (with $E_{\rm hc}$ fixed at the best-fit values mentioned above). The fitting results and the best-fit parameters are shown in Figure 5 and Table 1. By varying $E_{\rm lc}$ in fitting model (3), we also obtained $\Delta\chi^2$ versus $E_{\rm lc}$ (Figures 6(c) and (d)). Furthermore, we fitted the spectra using the warm-target model (fitting model (5), see Figures 6(a) and (b)), which in principle should show us the lower limits of $E_{\rm lc}$. The EM and temperature of the targets were derived from the cold-target fitting in the intervals just before the studied HXR peaks (02:38:10–02:38:20 UT and 04:02:50–04:03:00 UT for the two events), while the volume and loop length of the targets were estimated from RHESSI images during the soft X-ray peaks.

For the 2003 October 23 event, $E_{\rm lc}$ at minimum $\Delta\chi^2$ obtained from the cold- and warm-target models is 13.8 keV and 23.3 keV, respectively, both close to the lower cutoff energies detected from SEPs (∼15–22 keV). $E_{\rm lc}$ is better constrained in the warm-target model (21.8–24.9 keV at 1σ level). For the other event, $E_{\rm lc}$ at minimum $\Delta\chi^2$ obtained from the two models are 43.2 and 39.7 keV, both well constrained and close to the lower cutoff energies detected from SEPs (∼30–53 keV).

We also changed $E_{\rm hc}$ to find out how it affects the spectral fitting results. As shown in Table 1, the best-fit $E_{\rm lc}$ obtained using fitting model (2) (where $E_{\rm hc}$ is fixed at 32 MeV) for the two events show nearly no change. When $E_{\rm hc}$ of the two events are fixed at the lowest limits in Table 1, $E_{\rm lc}$ change to 21.5 and

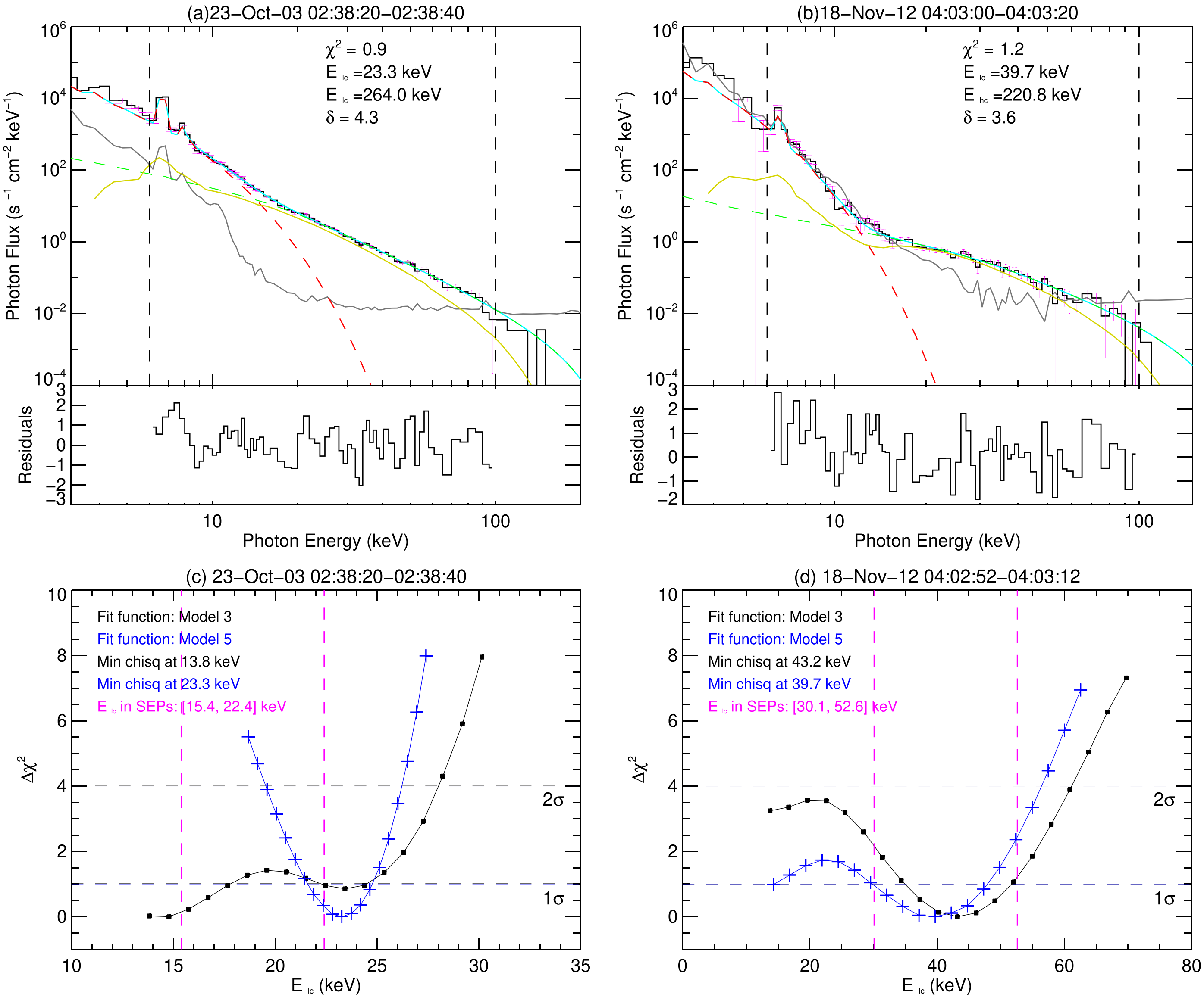

Figure 6. Panels (a) and (b): spectral fitting results of the events on 2003 October 23 event and 2012 November 18 using fitting model (5) f_vth+f_thick_warm +f_drm_mod+f_pileup_mod+f_albedo ($E_{\rm hc}$ is fixed at the best-fit value). The nonthermal components are shown as green dashed lines and other fit components are shown in the same way as Figure 3. Panels (c) and (d): $\Delta\chi^2$ vs. $E_{\rm lc}$ for the two SEP-related flare events from fitting model (3) f_vth+f_thick2_vnorm+f_drm_mod +f_pileup_mod+f_albedo ($E_{\rm hc}$ is fixed at the best-fit value) and fitting model (5). The $E_{\rm lc}$ ranges obtained from SEPs are shown in vertical lines.

36.1 keV, still in the range of those expected from the SEP results, but with larger uncertainties (5.2 and 24.9 keV). However, the residuals of the fitted spectra increase at high energies, and the electron indices δ become much harder (1.77 for the 2012 November 18 event). Therefore, $E_{\rm hc}$ obtained from fitting model (3) is most likely the overall best-fit value.

In order to compare the spectral indices more conveniently, we rebinned the electron distributions obtained from the fitted RHESSI spectra (Figures 5(b) and (e)) into the same energy bands of the SEP electron distributions, which take the effect of cutoffs into account. The rebinned electron distributions are shown in Figure 5, and the new slope $\beta_{\text{X-ray}}$ (red) is obtained from power-law fitting to the new distributions. The errors come from 100 calculations using a Monte Carlo method.

Note that the power-law slope β of electron distribution deduced from SEPs is smaller than the power-law slopes β (red) and δ derived from the thick-target fits for these two events. This is a common observation in flare-SEP events that was first reported by Krucker et al. (2007). It can be interpreted either in terms of differences in the acceleration or injection processes of the escaping and HXR-producing electron populations, or in terms of propagation effects that modify the spectrum of the SEPs. The drop of electron fluxes beyond the cutoff energies will affect the fitting of electron distribution, especially the power-law slope.

In contrast to this, our HXR fitting results show that the derived energy cutoffs, both low- and high-energy cutoffs, are very close to the lowest and highest energies detected in the in situ electrons. This novel observation strengthens the case for a close association of escaping and HXR-producing electrons and could be vital in achieving a better understanding of the differences between the two electron populations.

4. Conclusions

Whether or not low-energy cutoffs exist in flare-accelerated electrons is an important open question. We tried to find evidence from two populations of the accelerated electrons that propagate upward along opened field lines and downward along flare loops to the chromosphere, respectively. Unlike the previous studies also using X-ray data and SEP data, which focus on the comparison of slopes, we also consider the low- and high-energy cutoffs.

In the late impulsive X-ray bursts we selected, we observed the full spectral signature of low-energy cutoff that cannot be easily explained by other processes rather than the acceleration itself. The pulse pile-up and the albedo effect were accounted for in the spectral study and they made no significant effect on the cutoff energies and the spectral flattening in these events.

Return current energy losses may be another reason for the cause of spectral flattening as reported by Zharkova & Gordovskyy (2006), Holman (2012), and Alaoui & Holman (2017). But it requires large number of electrons (or number density) in the first place. We do not see such evidence so far in these events. Contrarily, the high low-energy cutoff derived here implies a small number of total electrons. Additionally, these flattenings cannot be simply represented by a single kappa distribution. The sources at low and high energies do not show a clear separation, meaning that they are likely from the same population of electrons. Therefore, the evident spectral flattening in these events is most likely to be caused by a high low-energy cutoff in the electron distribution.

We also showed the effect of high-energy cutoff on spectral shape. Compared with the cases where $E_{\rm hc}$ is fixed at 32 MeV, the free parameter $E_{\rm hc}$ can significantly change both the low-energy cutoff and electron distribution index in some cases. Therefore, high-energy cutoff is also an important parameter in spectra analysis and acceleration models. But a lower high-energy cutoff alone could not explain the spectral flattening in most events of this work.

The high low-energy cutoff means a relative deficit of electrons at low energies and low nonthermal energy carried by the energetic electrons. We used the DEM method to calculate the peak thermal energy of the late X-ray burst on 2015 April 16 and found that the total nonthermal energy of the late burst is still in the same order of the peak thermal energy.

The comparison of the electron distribution derived from X-ray spectra and SEP data showed the well-known fact that the spectral indices of these two electron populations are differing, which can be due to acceleration or propagation processes. However, we found that the lower and upper cutoff energies of these two electron populations are actually very consistent. This is an important new constraint for studies that try to model electron acceleration and transport. For the 2003 October 23 event, which has no evident spectral flattening, we found that the low-energy cutoff determined from the warm-target model is constrained better than that from the cold-target model.

The combination of X-ray data and SEP data is a powerful tool for diagnostic of energetic electrons accelerated in flares. The results we obtained here suggest (1) both low-energy cutoff and high-energy cutoff exist (at least in some events) and are directly related to the acceleration process; (2) both cutoff energies are important parameters for understanding X-ray spectral shape, electron distribution, and acceleration models; and (3) SEP data can provide useful information to constrain flare electron distributions, as fitting of HXR spectra alone does not always allow an unambiguous identification of the most appropriate fitting model.

RHESSI is a NASA Small Explorer Mission. SDO is a mission for NASA's Living with a Star program. This work is supported by the National Natural Science Foundation of China (grant Nos. 11820101002, U1631242, 11921003, U1731241, 41774183, 41861134033, U1931138) and the Strategic Pioneer Program on Space Science, Chinese Academy of Sciences (grant Nos. XDA15320300, XDA15016800, XDA15320104, XDA15052200). A.W. was supported by the German Space Agency DLR under grant No. 50 QL 1701. Y.S. also acknowledges the Jiangsu Innovation and Entrepreneurship Talents Program.

ORCID iDs

Fanxiaoyu Xia https://orcid.org/0000-0002-2630-4753
Yang Su https://orcid.org/0000-0002-4241-9921
Wen Wang https://orcid.org/0000-0003-4262-7269
Linghua Wang https://orcid.org/0000-0001-7309-4325
Alexander Warmuth https://orcid.org/0000-0003-1439-3610

References

Alaoui, M., & Holman, G. D. 2017, ApJ, 851, 78
Aschwanden, M. J., Caspi, A., Cohen, C. M. S., et al. 2017, ApJ, 836, 17
Aschwanden, M. J., Kontar, E. P., & Jeffrey, N. L. S. 2019, ApJ, 881, 1
Battaglia, M., Motorina, G., & Kontar, E. P. 2015, ApJ, 815, 73
Benz, A. O. 2017, LRSP, 14, 2
Bougeret, J. L., Kaiser, M. L., Kellogg, P. J., et al. 1995, SSRv, 71, 231
Brown, J. C. 1971, SoPh, 18, 489
Brown, J. C. 1973, SoPh, 28, 151
Cheung, M. C. M., Boerner, P., Schrijver, C. J., et al. 2015, ApJ, 807, 143
Christe, S., Hannah, I. G., Krucker, S., McTiernan, J., & Lin, R. P. 2008, ApJ, 677, 1385
Emslie, A. G., Dennis, B. R., Shih, A. Y., et al. 2012, ApJ, 759, 71
Feng, L., Wiegelmann, T., Su, Y., et al. 2013, ApJ, 765, 37
Fleishman, G. D., Pal'shin, V. D., Meshalkina, N., et al. 2016, ApJ, 822, 71
Gan, W. Q., Li, Y. P., & Chang, J. 2001, ApJ, 552, 858
Gan, W. Q., Li, Y. P., Chang, J., & Tiernan, J. M. 2002, SoPh, 207, 137
Handy, B. N., Tarbell, T. D., Wolfson, C. J., Korendyke, C. M., & Vourlidas, A. 1999, SoPh, 190, 351
Holman, G. D. 2003, ApJ, 586, 606
Holman, G. D. 2012, ApJ, 745, 52
Holman, G. D., Aschwanden, M. J., Aurass, H., et al. 2011, SSRv, 159, 107
Hudson, H. S. 2011, SSRv, 158, 5
Ireland, J., Tolbert, A. K., Schwartz, R. A., Holman, G. D., & Dennis, B. R. 2013, ApJ, 769, 89
Kašparová, J., & Karlický, M. 2009, A&A, 497, L13
Kašparová, J., Kontar, E. P., & Brown, J. C. 2007, A&A, 466, 705
Knight, J. W., & Sturrock, P. A. 1977, ApJ, 218, 306
Kontar, E. P., Brown, J. C., & McArthur, G. K. 2002, SoPh, 210, 419
Kontar, E. P., Dickson, E., & Kašparová, J. 2008, SoPh, 252, 139
Kontar, E. P., Jeffrey, N. L. S., & Emslie, A. G. 2019, ApJ, 871, 225
Kontar, E. P., Jeffrey, N. L. S., Emslie, A. G., & Bian, N. H. 2015, ApJ, 809, 35
Kontar, E. P., MacKinnon, A. L., Schwartz, R. A., & Brown, J. C. 2006, A&A, 446, 1157
Krucker, S., Battaglia, M., Cargill, P. J., et al. 2008, A&ARv, 16, 155
Krucker, S., Kontar, E. P., Christe, S., & Lin, R. P. 2007, ApJL, 663, L109
Krucker, S., & Lin, R. P. 2008, ApJ, 673, 1181
Landi, E., Del Zanna, G., Young, P. R., et al. 2006, ApJS, 162, 261
Lemen, J. R., Title, A. M., Akin, D. J., et al. 2012, SoPh, 275, 17
Li, Y. P., Gan, W. Q., & Feng, L. 2012, ApJ, 747, 133
Lin, R. P., Anderson, K. A., Ashford, S., et al. 1995, SSRv, 71, 125
Lin, R. P., Dennis, B. R., Hurford, G. J., et al. 2002, SoPh, 210, 3
Lysenko, A. L., Altyntsev, A. T., Meshalkina, N. S., Zhdanov, D., & Fleishman, G. D. 2018, ApJ, 856, 111
Oka, M., Ishikawa, S., Saint-Hilaire, P., Krucker, S., & Lin, R. P. 2013, ApJ, 764, 6
Oka, M., Krucker, S., Hudson, H. S., & Saint-Hilaire, P. 2015, ApJ, 799, 129
Petrosian, V. 2016, ApJ, 830, 28
Raymond, J. C., Krucker, S., Lin, R. P., & Petrosian, V. 2012, SSRv, 173, 197

Reid, H. A. S., & Ratcliffe, H. 2014, RAA, 14, 773
Saint-Hilaire, P., & Benz, A. O. 2005, A&A, 435, 743
Schwartz, R. A., Csillaghy, A., Tolbert, A. K., et al. 2002, SoPh, 210, 165
Su, Y., Holman, G. D., Dennis, B. R., Tolbert, A. K., & Schwartz, R. A. 2009, ApJ, 705, 1584
Su, Y., Veronig, A. M., Hannah, I. G., et al. 2018, ApJL, 856, L17
Sui, L., Holman, G. D., & Dennis, B. R. 2005, ApJ, 626, 1102
Sui, L. H., Holman, G. D., & Dennis, B. R. 2007, ApJ, 670, 862
Wang, L. 2009, PhD thesis, UC Berkeley
Wang, L., Lin, R. P., Krucker, S., & Mason, G. M. 2012, ApJ, 759, 69
Wang, W., Wang, L., Krucker, S., & Hannah, I. 2016, SoPh, 291, 1357
Warmuth, A., Holman, G. D., Dennis, B. R., et al. 2009a, ApJ, 699, 917
Warmuth, A., Mann, G., & Aurass, H. 2009b, A&A, 494, 677
Zharkova, V. V., Arzner, K., Benz, A. O., et al. 2011, SSRv, 159, 357
Zharkova, V. V., & Gordovskyy, M. 2005, SSRv, 121, 165
Zharkova, V. V., & Gordovskyy, M. 2006, ApJ, 651, 553